

The interaction of an oblique shock wave with a laminar boundary layer revisited. An experimental and numerical study

By G. DEGREZ†, C. H. BOCCADORO‡ AND J. F. WENDT

von Kármán Institute for Fluid Dynamics, Chaussée de Waterloo, 72,
B-1640 Rhode Saint Genèse, Belgium

(Received 6 September 1985 and in revised form 7 August 1986)

An investigation of an oblique shock wave/laminar boundary layer interaction is presented. The Mach number was 2.15, the Reynolds number was 10^6 and the overall pressure ratio was 1.55. The interaction has been demonstrated to be laminar and nominally two-dimensional. Experimental results include pressure distributions on the plate and single component laser-Doppler velocimetry velocity measurements both in the attached and separated regions.

The numerical results have been obtained by solving the full compressible Navier–Stokes equations with the implicit approximate factorization algorithm by Beam & Warming (1980). Comparison with experimental data shows good agreement in terms of pressure distributions, positions of separation and reattachment and velocity profiles.

1. Introduction

The main features of the oblique shock wave/laminar boundary layer interaction are well understood. The pioneering experiments by Chapman, Kuehn & Larson (1958) and Hakkinen *et al.* (1959) advanced and provided verification of the understanding. The interacting boundary layer theories by Crocco & Lees (1952) and Lees & Reeves (1964) gave an elegant explanation of the interaction and successfully predicted the surface pressure distributions obtained in the early experiments. These experiments and very few which followed did not, however, provide the detailed flow-field data that can be predicted by present day Navier–Stokes computational solutions. Indeed, because this configuration involves shocks and separated flow, two of the most difficult features to reproduce numerically, it was chosen as a test case by a number of computational fluid dynamicists (Skoglund & Gray 1969; MacCormack 1971; Hanin, Wolfshtein & Landau 1974; Beam & Warming 1978; MacCormack 1982; Dawes 1983). Also, due to its laminar character, it carries no uncertainty associated with turbulence modelling. Thus, the principal aim of this study was to provide a modern and complete set of experimental data (both flow-field and surface) to serve as reference for comparison with numerical solutions. In addition, a numerical solution of the Navier–Stokes equations was obtained and compared with the experimental data.

The use of traditional techniques, such as hot-wire anemometry or Pitot probes,

† Present address: Université de Sherbrooke, Cité Universitaire, Sherbrooke, Quebec J1K 2R1, Canada.

‡ Present address: Northrop Corporation, Advanced Systems Division, Pico Rivera, CA 90660, USA.

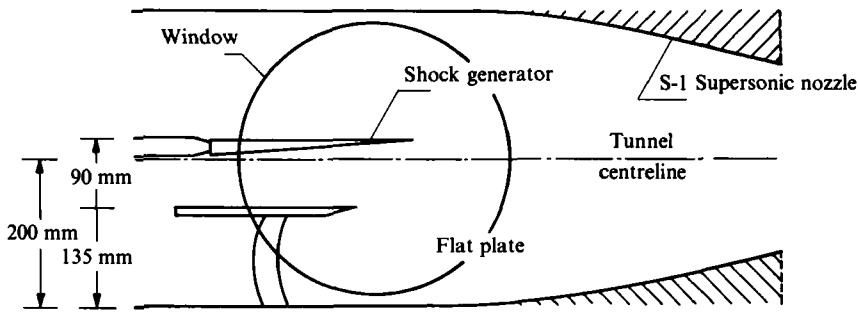


FIGURE 1. Schematic of wind-tunnel installation.

in examining regions of close surface proximity, widely differing velocities, compressible and reversed flows, has proved difficult and is largely responsible for the scarcity of high-quality data. The present investigation uses the laser-Doppler velocimeter (LDV) technique. It is ideally suited for this type of experiment because of its non-intrusive and linear nature and its capacity to provide very small probe volumes (< 0.2 mm diameter). The work of Modarress & Johnson (1979) on the turbulent boundary layer separation provides an example of the successful application of LDV in supersonic flows. The recent LDV work of Baroth & Holt (1983) provides one of the few examples of flow-field data for the laminar-separation case. The present experiment is one in a series of thin-boundary-layer studies at the von Kármán Institute (Degrez, Boccadoro & Wendt 1984; Boccadoro & Wendt 1984). Preliminary tests of two-dimensionality were conducted because of Green's (1970) observation, since supported by the work of Reda & Murphy (1973*a, b*), that large discrepancies in the scale of the separated region, particularly for flows beneath incident shocks, are probably the result of a three-dimensional perturbation or finite-span effect.

The numerical study of the interaction was based on the implicit approximate factorization algorithm of Beam & Warming (1978) for solving the time-dependent compressible Navier–Stokes equations. Implicit techniques have proved to represent major progress for the solution of the Navier–Stokes equations because of their improved stability properties with respect to the former explicit methods. This allows the use of larger timesteps and leads to faster convergence.

In §2, the experimental programme is described. The description of the computational study is presented in §3. In §§4 and 5 the experimental and numerical results are successively presented and discussed and §6 gives the conclusions of this study.

2. Experimental programme

2.1. Wind-tunnel and free-stream conditions

The experiments were carried out in the VKI S-1 40 cm \times 40 cm continuous supersonic wind tunnel with free-stream Mach number (M_∞) of 2.20. The stagnation pressure (P_t) and temperature (T_t) were respectively 0.107 bar \pm 2% and 293 K \pm 2% for the pressure distribution measurements, giving a nominal free-stream unit Reynolds number (Re_u) of 1.2×10^6 m $^{-1}$. During LDV tests, the conditions were slightly different; namely, $P_t = 0.123$ bar \pm 2% and $T_t = 303$ K \pm 2%. No flow-field unsteadiness was observed (by schlieren visualization) and all tests were conducted with adiabatic wall conditions.

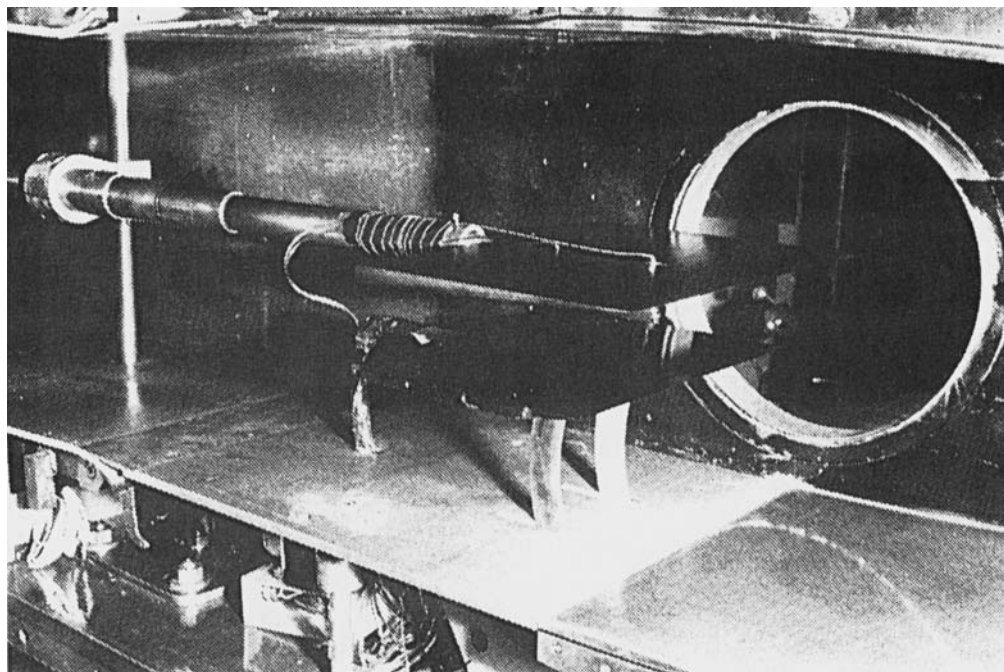


FIGURE 2. Model II installed in wind-tunnel section.

2.2. Test configuration

The test configuration consisted of a flat plate mounted through the test-section floor on a stand and a shock generator mounted on a sting. The schematic of the tunnel installation (figure 1) shows the respective positions of the flat plate and shock generator. There were actually two sets of flat plates and shock generators, differing in span, which were respectively 200 mm (model I) and 320 mm (model II) for the plate, 250 mm (model I) and 360 mm (model II) for the shock generator. Plate and shock generator leading edges were sharp with leading-edge thicknesses of less than 0.1 mm. Triangular side plates could be mounted on the flat plates about their centreline at interspan distances of 144 mm and 200 mm (model I) and 200, 240, 280 and 320 mm (model II). The shock generator compression angle was 3.75° . Model II is shown installed in the wind tunnel in figure 2.

Both models were instrumented with a row of pressure taps on the centreline and additional taps off-centreline to check for flow uniformity.

2.3. Measurement techniques

2.3.1. Surface pressure measurements

Model pressures were sensed by a system of rotary scanning valves and pressure transducers. A 0.5 PSID (3500 N m^{-2}) Statham transducer, referenced to a test-section wall pressure (P_w), measured all model pressures via a network of scanning valves. Susceptibility to pressure leaks was reduced by locating the transducer and the scanning valves in a chamber underneath the test-section floor. This chamber had an ambient pressure of the order of the pressure being measured by the transducer. A second Statham transducer of 1 PSI (7000 N m^{-2}), referenced to an evacuated reservoir, measured P_w . This transducer was located outside the tunnel. The vacuum

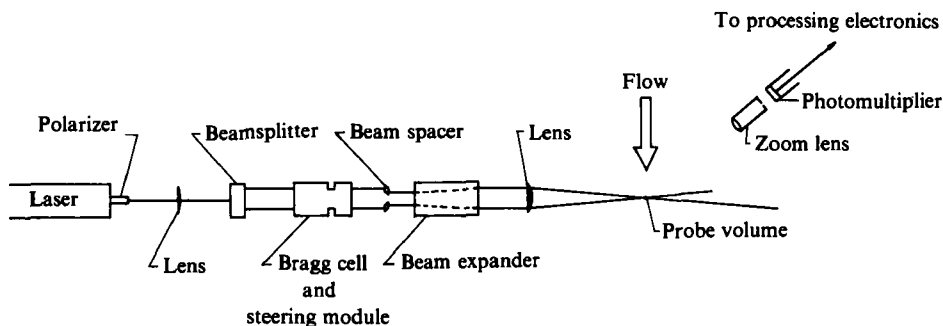


FIGURE 3. Schematic of LDV system.

Laser velocimetry parameters

Laser wavelength, λ	0.5145 μm
Beam diameter, D_{e-2}	3.40 mm
Focal length of lens, f	750 mm
Angle of intersection, 2ϕ	3.82°
Beam separation, d	50 mm
Fringe spacing, d_f	7.72 μm
Width of probe volume, d_m	144 μm
Beam waist, d_{e-2}	144 μm
Length of probe volume, l_m	4.33 mm
Number of fringes (unshifted), N_{fr}	18.7

Equations for laser velocimetry system

$$\phi = \arctan(d/2f) \quad (1)$$

$$d_f = \lambda/2 \sin \phi \quad (2)$$

$$d_{e-2} = 4\lambda f/\pi D_{e-2} \quad (3)$$

$$d_m = d_{e-2}/\cos \phi \quad (4)$$

$$l_m = d_{e-2}/\sin \phi \quad (5)$$

$$N_{fr} = d_m/d_f \approx 4d/\pi D_{e-2} \quad (6)$$

$$U = d_f \nu_D = d_f(\nu_p - \nu_B) \quad (7)$$

where

U = velocity perpendicular to fringes

ν_D = Doppler frequency

ν_p = processor frequency

ν_B = Bragg frequency

TABLE 1. Laser-velocimetry parameters and equations

reservoir pressure varied between 0.2 and 0.4 mmHg (27 and 57 N m⁻²) for all runs. It was measured with a Thermotron vacuum meter for tests with model I and a McLeod vacuum gauge for the test with model II. The two Statham transducers were calibrated under atmospheric conditions against a Betz water manometer.

2.3.2. Stagnation pressure and free-stream conditions

The tunnel stagnation pressure was measured in the stagnation chamber with a Pitot probe, using a mercury manometer. The free-stream Mach number (M_∞) was determined during a preliminary test using a Pitot probe connected to another mercury manometer. The probe had a 6 mm outer diameter and was located 25 mm

above the test section centreline (where the shock generator was located normally). The Rayleigh Pitot probe relationship was then used. The free-stream static pressure (p_∞) was computed from the isentropic relationship using tunnel stagnation pressure and free-stream Mach number.

2.3.3. Laser velocimeter

The laser velocimeter was a single velocity component, dual beam, fringe mode system with forward scatter light collection. A schematic of the system is shown in figure 3, and its parameters including probe volume dimensions are given in table 1. Further details about the set-up can be found in Boccadoro & Wendt (1984).

The flow was seeded with a mist of fine oil droplets produced by a Norgren aerosol generator ('Microfog' model). Vorropoulos & Wendt (1983) measured the size distribution of droplets produced by the generator with an OEI iso-kinetic sampling probe. The mean droplet diameter was $0.45 \pm 0.05 \mu\text{m}$. This diameter would satisfy the criterion reviewed by Durst, Melling & Whitelaw (1976) for particles to adequately follow high subsonic and supersonic flows. Experimental results led us to question this value of particle size for the present test conditions.

Runs were limited to about two hours because of oil formation on the flat plate and test-section windows. The tiny oil beads that formed on the plate at the end of a run, however, produced a visualization of the separation line which enabled a confirmation of the separation location discussed in §4.

2.4. Flow characteristics

The test configuration and conditions which have been described above were selected so that:

- the interaction would produce an appreciable separated recirculating flow region;
- the flow would remain laminar throughout the interaction region;
- the flow would be two-dimensional.

The first two points were established *a priori* using the results of Burgio & Ginoux (1970) and Ginoux (1968). Burgio & Ginoux showed the existence of an extended region of separation for the present test conditions, and demonstrated its laminar character using the criterion set forth by Ginoux – stating that the separation length and maximum pressure gradient at separation increase with free-stream Reynolds number (Re_u) for the laminar case and decrease with Re_u for the transitional case. Additional evidence of laminarity was provided by the sharply defined edges of the boundary layers observed in schlieren and shadowgraph visualizations and by the shape of the velocity profiles to be presented. A schlieren photograph, showing the entire interaction is presented in figure 4, together with a schematic identifying the major flow features.

The two-dimensional character of the flow could not be established *a priori* for lack of information about this issue. An extensive study was therefore performed. The results are presented in §4.

3. Computational study

The numerical results were obtained by time integration of the full compressible Navier–Stokes equations using the implicit approximate factorization algorithm of Beam & Warming, until a steady solution was obtained. The algorithm has been thoroughly studied (Warming & Beam 1978, 1979; Beam & Warming 1980) and extensively described in its original Cartesian form (Beam & Warming 1978) and in

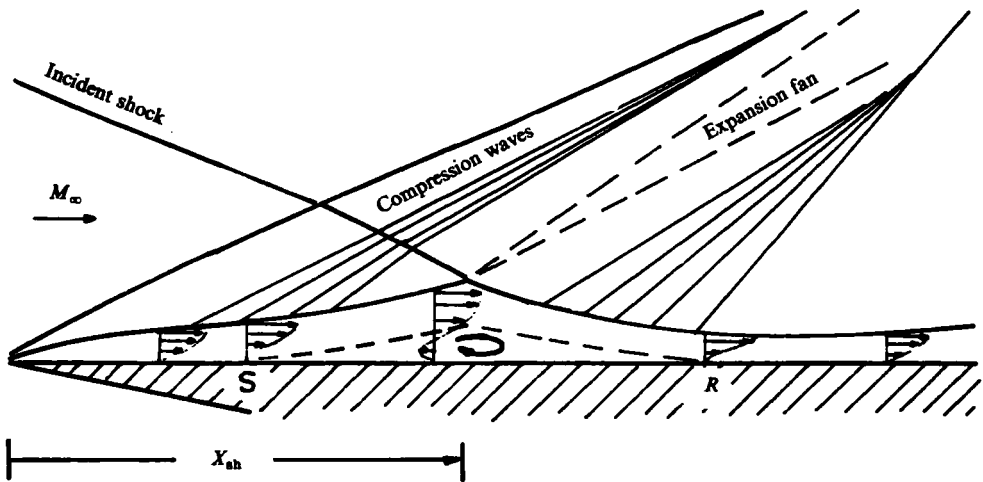
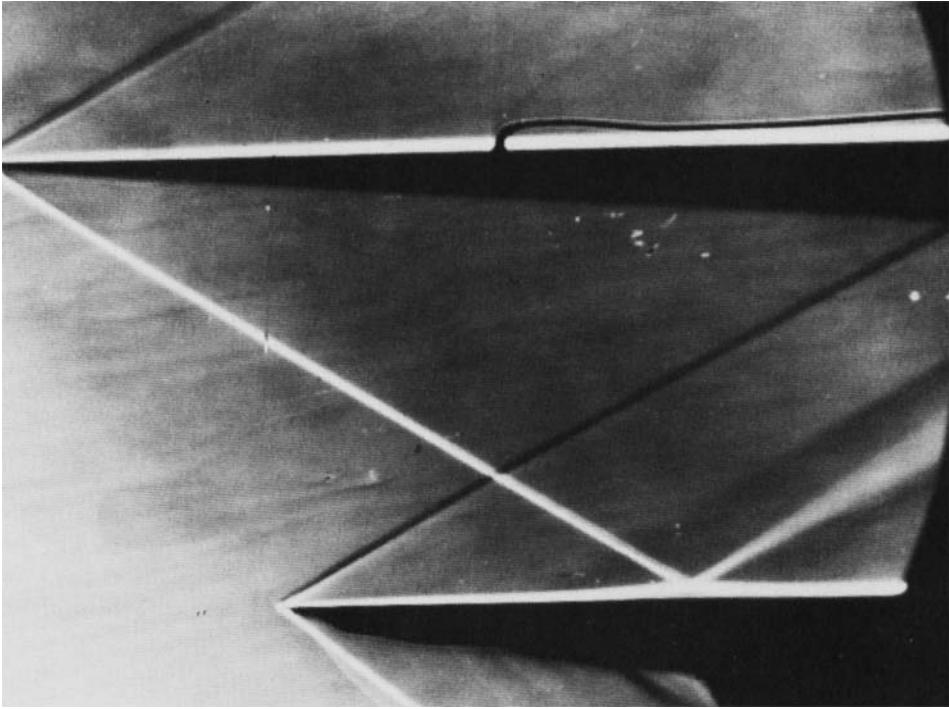


FIGURE 4. Schlieren visualization and schematic of the flow field.

general curvilinear coordinates (Thomas 1979). This latter form was used in the code developed at the von Kármán Institute which is presented in detail by Degrez (1984). Its main features are outlined below.

The Navier–Stokes equations written in generalized coordinates and in non-dimensional form are

$$\frac{\partial \hat{q}}{\partial \tau} + \frac{\partial \hat{f}}{\partial \xi} + \frac{\partial \hat{g}}{\partial \eta} = \frac{1}{Re} \left(\frac{\partial \hat{\sigma}}{\partial \xi} + \frac{\partial \hat{\theta}}{\partial \eta} \right), \quad (1)$$

where $\hat{q} = JU$, $\hat{f} = \hat{\xi}_t U + \hat{\xi}_x F + \hat{\xi}_\eta G$, $\hat{g} = \hat{\eta}_t U + \hat{\eta}_x F + \hat{\eta}_y G$,

$$Re = \frac{c_\infty X_{sh} \rho_\infty}{\mu_\infty}, \quad \hat{\xi}_t = J \xi_t$$

and similarly for $\hat{\xi}_x, \hat{\xi}_y, \dots$, and J is the Jacobian of the inverse transformation

$$U = \begin{pmatrix} \rho' \\ \rho' u' \\ \rho' v' \\ \rho' E' \end{pmatrix}, \quad F = \begin{pmatrix} \rho' u' \\ (p'/\gamma) + \rho' u'^2 \\ \rho' u' v' \\ (\rho' E' + (p'/\gamma)) u' \end{pmatrix}, \quad g = \begin{pmatrix} \rho' v' \\ \rho' u' v' \\ (p'/\gamma) + \rho' v'^2 \\ (\rho' E' + (p'/\gamma)) v' \end{pmatrix}, \quad (2)$$

where primes denote non-dimensional quantities, with the normalizing quantities being ρ_∞ for density, c_∞ for velocity, c_∞^2 for energy per unit mass, p_∞ for pressure, T_∞ for temperature, X_{sh} for length and X_{sh}/c_∞ for time. The perfect gas law relates thermodynamic quantities. The viscous fluxes can be calculated by similar relations. Their expressions are given by Thomas (1979).

These equations are central-space-differenced and implicitly advanced in time. Linearizations and approximate factorization are performed to obtain the final scheme:

$$\left\{ I + \theta \Delta \tau \left[\frac{\partial}{\partial \xi} \left(\hat{F} - \frac{\hat{S}}{Re} \right) \right] \right\} \left\{ I + \theta \Delta \tau \left[\frac{\partial}{\partial \eta} \left(\hat{G} - \frac{\hat{T}}{Re} \right) \right] \right\} \Delta \hat{q} \\ = \Delta \tau \left[-\frac{\partial \hat{f}}{\partial \xi} - \frac{\partial \hat{g}}{\partial \eta} + \frac{1}{Re} \left(\frac{\partial \hat{\sigma}}{\partial \xi} + \frac{\partial \hat{\theta}}{\partial \eta} \right) \right], \quad (3)$$

where $\hat{F}, \hat{G}, \hat{S}, \hat{T}$ are Jacobians of inviscid and viscous fluxes and derivatives stand for their central difference representations. For the present steady-state computation, the first-order scheme corresponding to $\theta = 1$ was used because of its improved dissipation properties with respect to the second-order scheme ($\theta = \frac{1}{2}$). Fourth-order dissipation terms were appended to the right-hand side of equation (3) to damp short wavelengths that are not dissipated by the implicit scheme (Beam & Warming 1978; Thomas 1979).

Due to the simplicity of the configuration, the grid was generated analytically. There were 50 points uniformly spaced in the $x(\xi)$ -direction and 36 points stretched exponentially away from the plate in the transverse direction. The latter stretching was performed to resolve the boundary layer along the plate. The computational domain is shown in figure 5. Subsequently, a halved mesh system of 100×71 points was also used for verification of the validity of numerical results. The computation was performed using a maximum Courant (CFL) number of 178. Convergence was reached in less than 150 iterations, i.e. 1 h of computing time on a DEC VAX 11/780 computer.

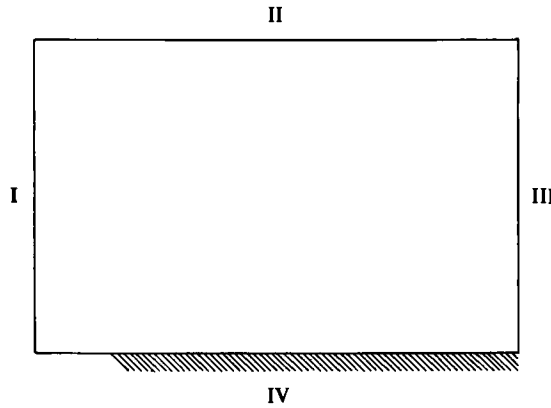


FIGURE 5. Computational domain.

4. Experimental results

4.1. Two-dimensionality study

The condition of two-dimensionality was assessed against the criterion set forth by Holden (Hankey & Holden 1975) that changes performed at spanwise extremities of the model do not influence the centreline properties. This requirement is stronger than that of uniformity of flow properties over a certain span of the model, as discussed by Holden. Modelling Lewis, Kubota & Lees' (1968) work with a supersonic compression corner, side plates large enough to contain the entire separation interaction were mounted on the model at various inter-plate spans and centreline pressure distributions were measured. For the compression corner, Lewis *et al.* (1968) and Sfeir (1970) found that a limiting pressure distribution was obtained when the inter-plate span exceeded the shock impingement distance from the plate leading edge; in other words, when the aspect ratio (AR), defined as the ratio of the inter-plate span to X_{sh} , was greater than 1. This was found true for Mach numbers of 2.5 and 4 with compression corner angles up to 15° . In our study, model I was tested with aspect ratios of 1.8 and 2.5 and model II with aspect ratios of 2, 2.5, 3.5 and 4. The configuration with no side plates was tested also on both models.

Figure 6 shows the centreline pressure distributions on model I for three cases ($AR = 1.8, 2.5$, no side plates). The pressures have been normalized by the minimum pressure (p_0) just upstream of the interaction and the streamwise coordinate x by X_{sh} . A considerable difference is noted between the $AR = 1.8$ and 2.5 tests on the upstream side of the interaction. It is as much as 8% of the overall interaction pressure difference ($(p_f - p_0)/p_0 = 0.45$ (p_f denotes the final downstream uniform pressure)). An additional 3% difference occurred when the side plates were removed. This trend of decreased extent in the separated region with increased aspect ratio and side plate removal is identical to that noted by Lewis. However, no clear limit was demonstrated and model II was constructed so that larger aspect ratios could be examined.

Figure 7 shows the results of aspect ratio variation for model II. All curves fall within a limit of 6% with respect to the 0.50 overall pressure difference. However, no pattern is noticed and the spread is within the upper limit of experimental scatter (see below). A curve representing this 'limiting two-dimensional pressure distribution' (to within a range indicated by vertical bars) can be drawn in as shown.

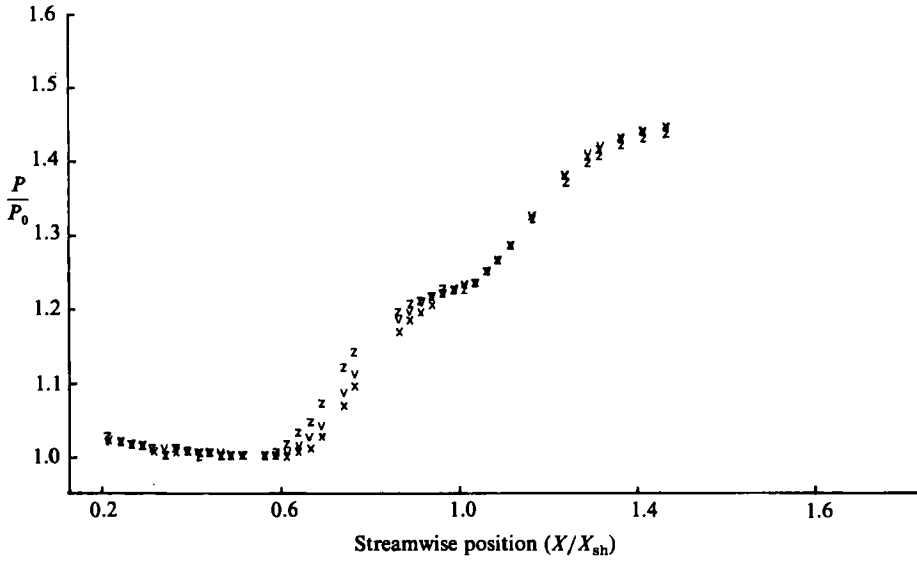


FIGURE 6. Pressure distributions for different side plates settings (model I). Aspect ratio: \times , 2.5 (side plates off); v , 2.5; z , 1.8. Model I: $M_\infty = 2.20$; $Re_{X_{sh}} = 0.96 \times 10^6$; $X_{sh} = 80$ mm.

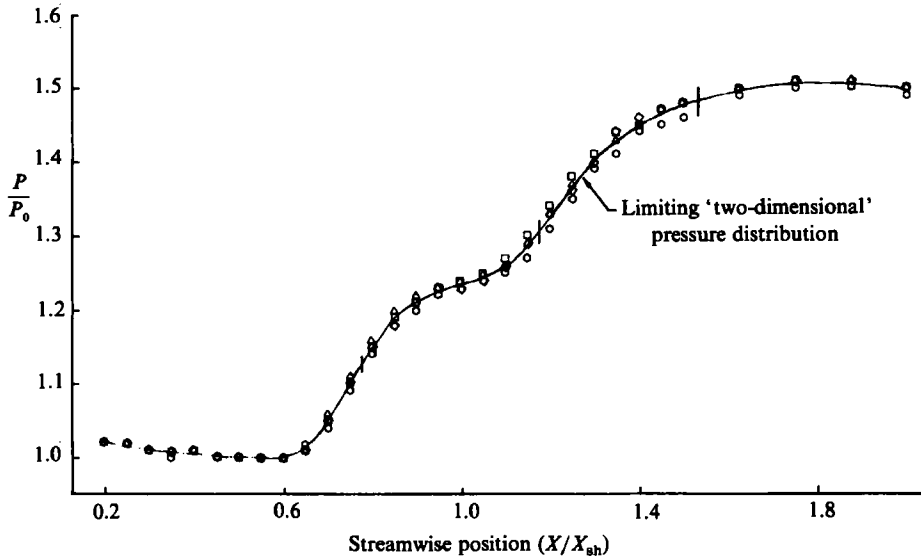


FIGURE 7. Pressure distributions for different side plates settings (model II). Aspect ratio: \square , 4.0; \diamond , 3.5; \circ , 3.0; \triangle , 2.5. Model II: $M_\infty = 2.20$, $Re_{X_{sh}} = 0.96 \times 10^6$; $X_{sh} = 80$ mm.

When the side plates were removed (figure 8), the pressure decreases, as was observed with model I. Smaller differences with the 'two-dimensional distribution' were expected for this larger span model, but these are seen actually to be larger. A possible explanation is that the model is encountering increased non-uniformities in the test-section flow field as the tunnel walls are approached, which are isolated when the side plates are installed.

Figure 9 shows spanwise pressure distributions for aspect ratio variation

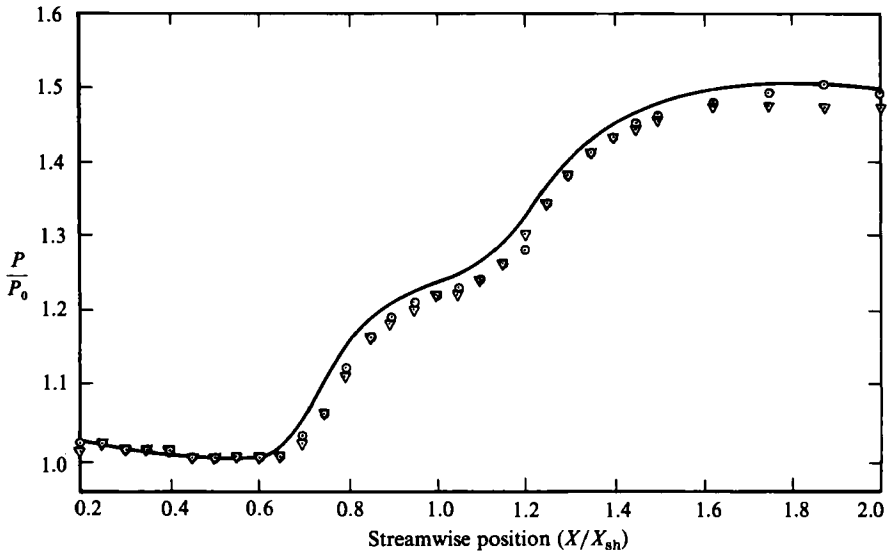


FIGURE 8. Pressure distributions with side plates off (model II). —, two-dimensional pressure distribution; \odot , side plates off; ∇ , small side plates. Model II: $M_\infty = 2.20$; $Re_{X_{sh}} = 0.96 \times 10^5$; $X_{sh} = 80$ mm; $AR = 4.0$.

($AR = 2.5, 4.0$, no side plates). All pressures have been normalized to p_0 on the centreline. The uniformity is seen to be good for all test cases, which agrees with Holden's aforementioned observation, that spanwise uniformity is a necessary but not sufficient condition of two-dimensionality.

The above results lead to the following conclusions: the flow over the centreline region of the model can be considered two-dimensional for aspect ratio of 2.5 or greater with side plates installed. This limit occurs at an aspect ratio much larger than obtained by Lewis *et al.* and Sfeir for compression-corner interactions, which supports Green's observation (1970) that the effect of experimental geometry is less pronounced for compression-corner interactions.

4.2. Velocity measurements

The velocity measurements were performed following the pressure measurements. The side plates were removed to eliminate the added complication of a transparent side plate. Two-dimensionality in terms of the above criterion can therefore not be claimed for the flow-field measurements obtained. However, the differences from the limiting pressure distribution observed in figure 9 when the side plates are removed are small compared to the controversial discrepancies which prompted Green's (1970) plea for more detailed experiments. The velocity profiles so obtained can be said to be free from large end effects and as such should provide a valuable contribution to an area where such data are genuinely scarce.

The mean velocity profiles obtained in the separated region are presented in figure 10. The velocities (U) are normalized by the local velocity measured at the edge of the boundary layer (U_e). Profiles are positioned along the x -axis according to their streamwise location (x/X_{sh}) on the plate. Profiles were also measured upstream and downstream of the separated region, but are not presented here to keep figure 10 as clear as possible. Two such profiles will be presented in §5 and compared with the results of the numerical computation.

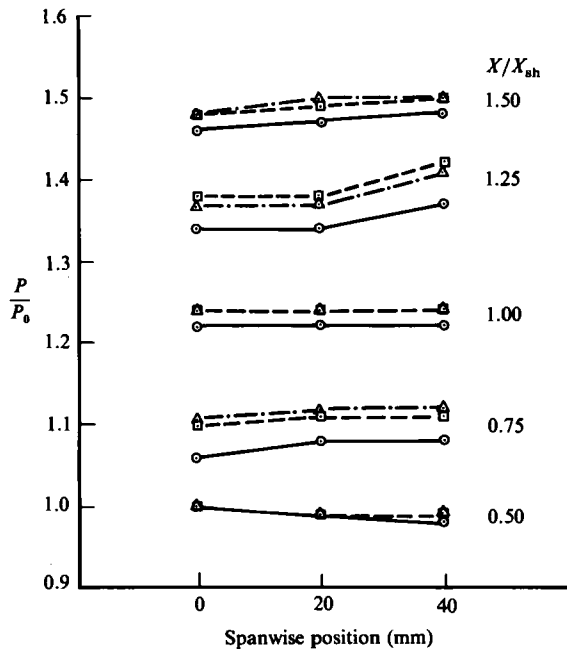


FIGURE 9. Spanwise pressure distributions under various conditions. Aspect ratio: \odot , 4.0 (side plates off); \square , 4.0; \triangle , 2.5. Model II: $M_\infty = 2.20$; $Re_{X_{sh}} = 0.96 \times 10^5$; $X_{sh} = 80$ mm.

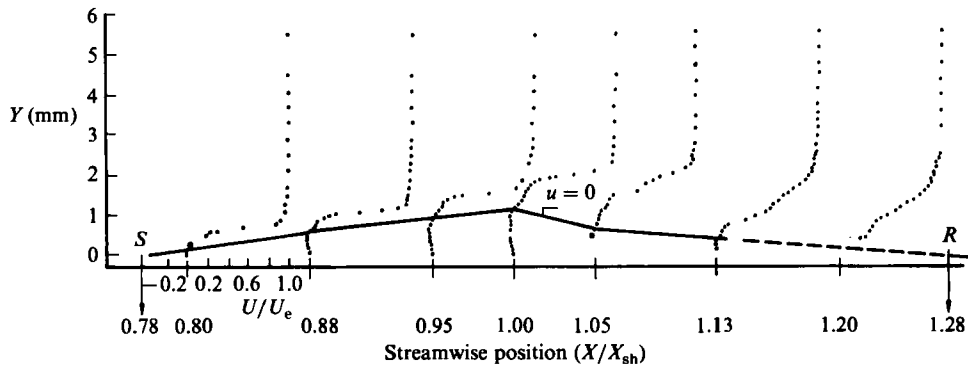
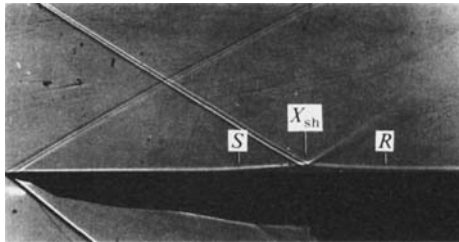


FIGURE 10. Velocity profiles in separated region. $M_\infty = 2.20$; $Re_{X_{sh}} = 1.12 \times 10^5$; $X_{sh} = 80$ mm.

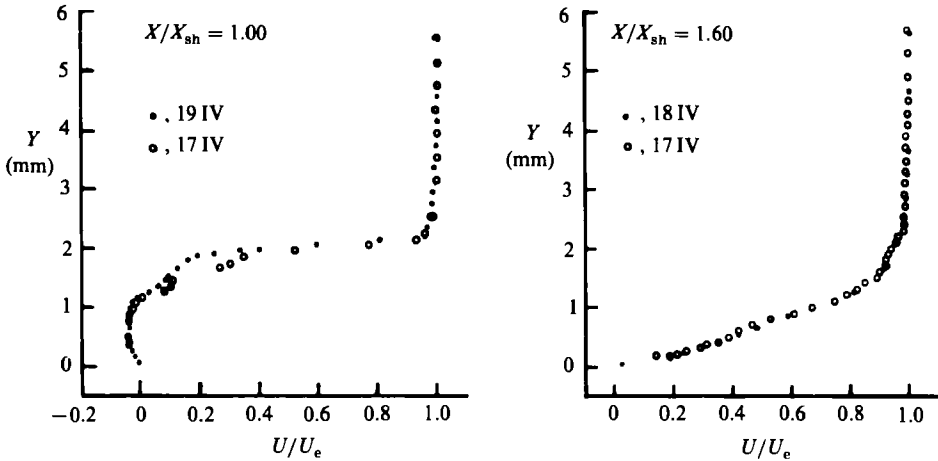


FIGURE 11. Repeatability of velocity measurements.

The general shape of the velocity profile is in agreement with the known structure of the interaction. Upstream of the shock impingement point, the boundary layer thickens, together with the reverse flow region. Downstream, the boundary-layer thickness decreases due to the turning of the outer flow when passing through the reflected expansion at the impingement point (see shadowgraph). From the velocity profiles was drawn a line of points where $u = 0$. This line was extrapolated linearly up to the location of separation (S) and reattachment (R). S occurs at $x/X_{sh} = 0.78$ or $x = 62 \text{ mm} \pm 1 \text{ mm}$, and R at 1.28 or $102 \text{ mm} \pm 2 \text{ mm}$. In the shadowgraph (figure 10) the S and R locations from the profiles have been marked. They are seen to agree well with the flow pattern exhibited in the photograph. In addition, the position of separation was confirmed by the position of oil accumulation after a long run, mentioned in §2.

The surface zero position ($y = 0$) was determined from extrapolation of selected profiles (those having good spatial resolution near $y = 0$) using the no-slip condition at the surface. Once obtained, the reference coordinates from the traversing table could be corrected and all profiles could be plotted. Alignment of the traversing table and its coordinate system with respect to the flat plate was assessed through a procedure fully described by Boccadoro & Wendt (1984). This permitted the determination of the $y = 0$ position at each station. Measurements were obtained to within 0.1 mm from the surface in the separated region (see figure 10) and downstream, and to within 0.2 mm for the profiles upstream.

4.3. Measurement repeatability

Pressure measurements on the same configuration (same AR) were repeated systematically on different days. The scatter of data was within 4% of the overall pressure increase in the forward part of the interaction and within 8% in the downstream region.

Because of the possible influence of the operating technique itself (such as filter switching, photomultiplier gain, counter scaling factor, etc.), numerous repeat velocity measurements were conducted. Comparisons are presented in figure 11; the agreement is good.

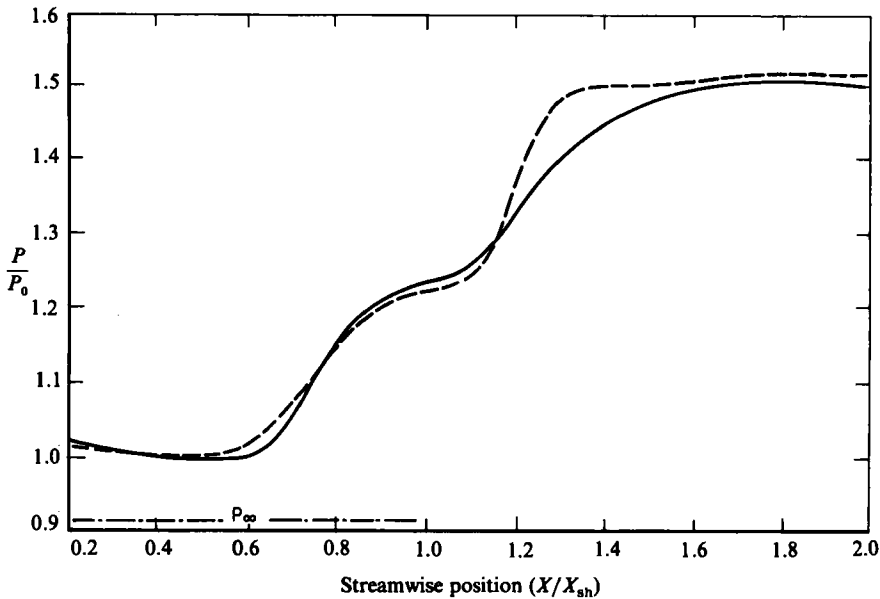


FIGURE 12. Comparison of computed and measured pressure distributions. —, two-dimensional pressure distribution. $M_\infty = 2.20$ ($M_\theta = 2.5$); $Re_{X_{sh}} = 0.96 \times 10^5$; $X_{sh} = 80$ mm. ---, computation. $M_\infty = 2.15$; $Re_{X_{sh}} = 1.0 \times 10^5$; $X_{sh} = 80$ mm; $\theta_1 = 30.8^\circ$.

5. Numerical results and comparison with experimental data

5.1. Pressure distribution

Figure 12 shows a comparison of the computed pressure distribution (using the Navier–Stokes code described in §3) and the limiting two-dimensional pressure distribution identified in the experiments. In addition, the free-stream pressure level is shown, calculated from stagnation pressure and free-stream Mach number. From the figure, it can be seen that p_0/p_∞ was typically 1.10 during the experiment. This value is 7% higher than the value 1.03 predicted by weak interaction theory (Kubota & Ko 1967). This discrepancy could be caused by the flat plate having a slight incidence (less than 1°) with respect to the flow, due to local flow angularity. Non-uniformity in the test-section Mach number (of about 2%) could also account for this discrepancy. The possibility of a systematic error in the measurement of the absolute level of p_0 was discarded after numerous checks using various types of instrumentation. This is the reason why a Mach number of 2.15 was used in the calculation, as this would account for $p_0/p_\infty = 1.1$ (where p_∞ was calculated with $M_\infty = 2.2$). It should be stressed that this value is confirmed by the measurement of the free-stream velocity, which was 540 m s^{-1} . Because of the high sensitivity of the overall pressure rise to the incident shock angle, this value (which is an input of the computer code) was selected so as to match the measured pressure rise. This corresponds to a theoretical shock-wave angle of 30.8° . It is worth noting that this is very close to the value calculated from the intentionally measured pressure on the shock generator, using oblique-shock-wave theory (30.6°). Computed and measured pressure distributions agree well (within experimental scatter) in the fore part and plateau region of the interaction. The calculation predicts, however, a steeper pressure gradient at reattachment. No explanation can be provided for this dis-

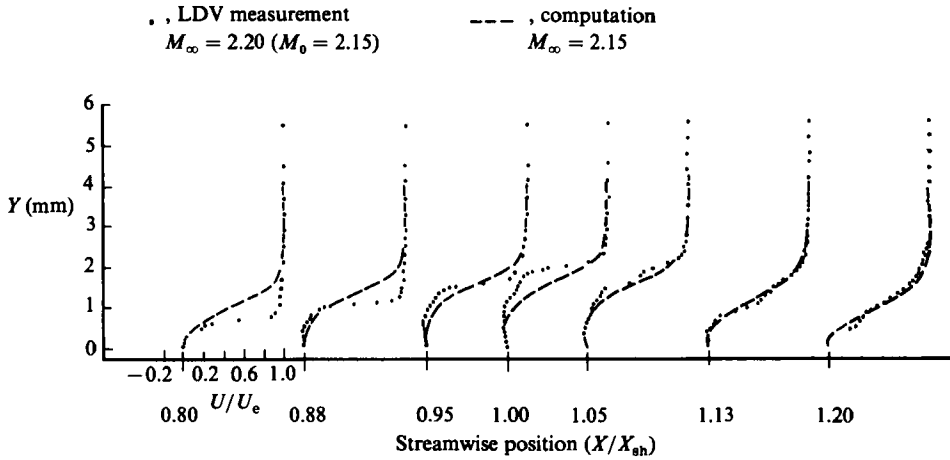


FIGURE 13. Comparison of computed and measured velocity profiles (separated region).

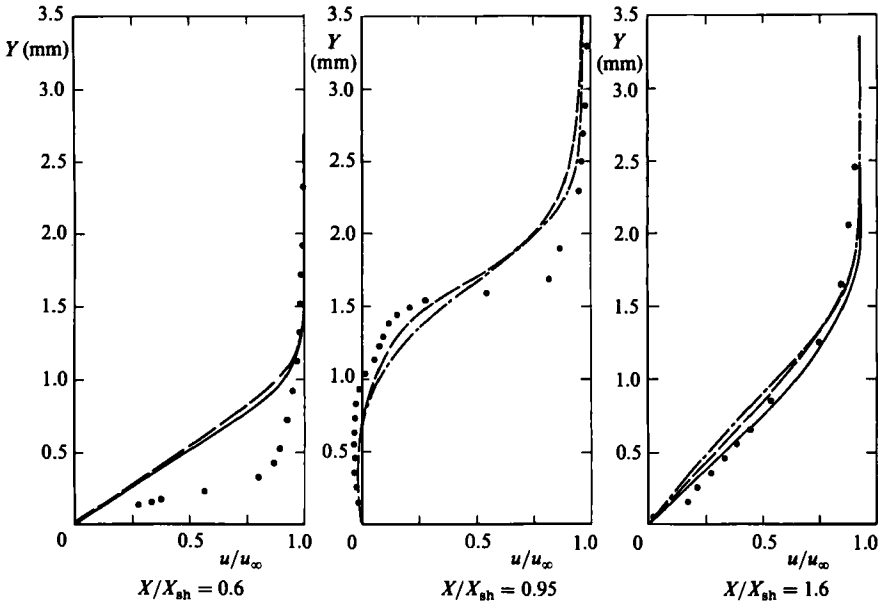


FIGURE 14. Comparison of velocity profiles: experimental, computed (original+halved grid), compressible boundary-layer theory. —, original mesh; ---, finer mesh; —·—, Chapman-Rubensin; ●, experiment.

crepancy but a similar behaviour was observed in Carter's (1972) calculation of Lewis *et al.*'s (1968) compression-corner experiments.

5.2. Velocity profiles – separation – reattachment

Figure 13 shows the comparison of measured and computed velocity profiles in the separated region. Agreement is excellent on the downstream side but worsens upstream, where experimental velocities are seen to rise more rapidly to U_e than the gradual behaviour predicted by the computation. At least two possibilities exist which might cause this discrepancy: either the computation grid is too coarse, so that

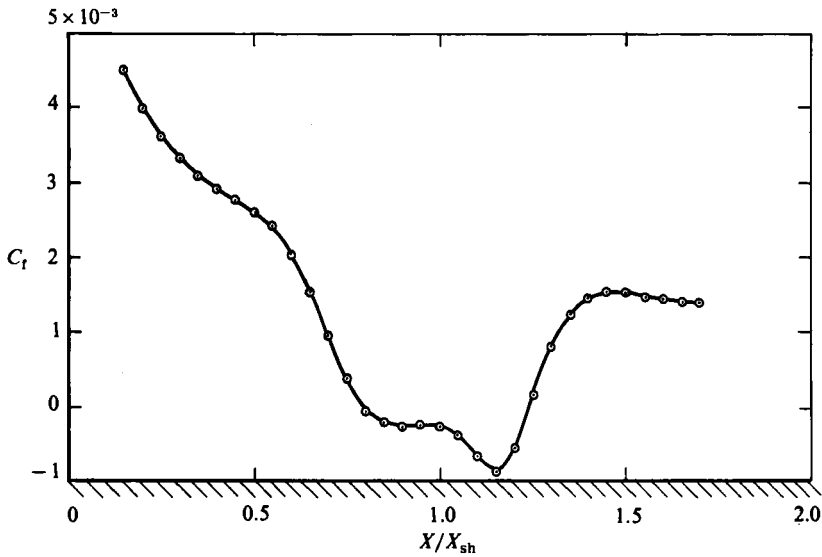


FIGURE 15. Distribution of skin-friction coefficient. Laminar flow.
 $M = 2.15$; $Re_{x_{sh}} = 1 \times 10^6$; $X_{sh} = 8 \times 10^{-2}$ m.

it does not resolve the experimentally observed sharp velocity gradient, or the experimental velocity measurements are in error in the upstream part of the flow. This might be due to the seeding particles not following the flow, despite the previous success of Vorropoulos & Wendt's measurement profiles (see §2).

The appropriateness of the computational mesh was checked by halving the grid. Figure 14 shows the results of both computations compared with the experiments for a station upstream of the interaction region, one in the separated region and one downstream. In addition for upstream and downstream profiles, the velocity profiles calculated by the well-established theory of Chapman & Rubesin (1949) are shown. It clearly appears that the resolution of the original mesh was sufficient, since no major differences exist between the computational results. Furthermore, the computed profiles agree very well with the Chapman-Rubesin profiles both upstream and downstream of the interaction.

Therefore, it seems that the origin of the discrepancies lies in an experimental error. The behaviour of the seeding particles is currently being investigated (Schütz 1985). Early results indicate that the particle size is larger than that measured by Vorropoulos & Wendt for these supersonic operating conditions, which supports the second possible explanation set forth above.

The calculated skin-friction distribution is plotted in figure 15. Separation and reattachment points are those positions where the skin-friction coefficient vanishes. The calculation predicts separation at $x/X_{sh} = 0.79$ and reattachment at $x/X_{sh} = 1.24$. These values are in close agreement with the experimental values quoted in §4 ($S: x/X_{sh} = 0.78$, $R: x/X_{sh} = 1.28$).

6. Conclusions

A combined experimental/numerical study of an incident oblique shock wave/laminar boundary layer interaction was performed. The Mach number was 2.15, the Reynolds number was 10^6 and the overall pressure ratio was 1.55.

A preliminary two-dimensionality study was performed, which showed that the

configuration with side plates could be considered two-dimensional for aspect ratios greater than 2.5.

The velocity measurements were obtained, both in the separated and attached flow regions, within 0.1 mm from the wall. The maximum height of the separated boundary layer was just over 3 mm. The length of separation was 40 mm. Separation and reattachment locations obtained from a linear extrapolation of the zero velocity lines agree closely with the shadowgraph visualization.

The numerical results were obtained by solving the full compressible Navier–Stokes equations with the implicit approximate factorization algorithm by Beam & Warming. Comparison with experimental data shows good agreement in terms of pressure distributions, positions of separation and reattachment, and downstream velocity profiles. Halving the grid showed the correctness of computed velocity profiles in the upstream region, which indicates that discrepancies observed with experiments on those profiles are due to an experimental error, probably caused by the velocity lag of finite-sized seed particles.

The present study was partially supported by the US Air Force Office of Scientific Research under Grant AFOSR 83-0273 monitored by Dr James Wilson. Very useful remarks from Professors J. J. Ginoux and M. L. Riethmuller concerning the experiment are gratefully acknowledged.

REFERENCES

- BAROTH, E. C. & HOLT, M. 1983 Investigation of supersonic flow in a compression corner by laser Doppler anemometry. *Exp. Fluids* **1** (4), 195–203.
- BEAM, R. M. & WARMING, R. F. 1978 An implicit factored scheme for the compressible Navier–Stokes equations. *AIAA J.* **16** (4), 392–402.
- BEAM, R. M. & WARMING, R. F. 1980 Alternating direction implicit methods for parabolic equations with a mixed derivative. *SIAM J. Sci. Stat. Comput.* **1**, 131–159.
- BOCCADORO, C. H. & WENDT, J. F. 1984 Investigation of an oblique shock wave/laminar boundary layer interaction using LDV. *von Kármán Institute TN* 152.
- BURGIO, C. & GINOUX, J. J. 1970 Comparison between shock wave/boundary layer interactions caused by either incident shocks or ramps. *von Kármán Institute PR* 70-226.
- CARTER, J. E. 1972 Numerical solution of the Navier–Stokes equations for the supersonic laminar flow over a two-dimensional compression corner. *NASA TR* R 385.
- CHAPMAN, D. R. & RUBESIN, M. W. 1949 Temperature and velocity profiles in the compressible laminar boundary layer with arbitrary distribution of surface temperature. *J. Aero. Sci.* **16** (9), 547–565.
- CHAPMAN, D. R., KUEHN, D. M. & LARSON, H. K. 1958 Investigation of separated flows in supersonic and subsonic streams with emphasis on the effect of transition. *NACA TR* 1356.
- CROCCO, L. & LEES, L. 1952 A mixing theory for the interaction between dissipative flows and nearly isentropic streams. *J. Aero. Sci.* **19** (10), 649–676.
- DAWES, W. N. 1983 Efficient implicit algorithm for the equations of 2D viscous compressible flow: application to shock boundary layer interaction, *Intl J. Heat & Fluid Flow* **4** (1), 17–26.
- DEGREZ, G. 1984 Etude théorique et expérimentale d'interactions bi- et tridimensionnelles entre ondes de choc et couches limites laminaires. Thèse de Doctorat, Université Libre de Bruxelles.
- DEGREZ, G., BOCCADORO, C. H. & WENDT, J. F. 1984 LDV velocity measurements in thin laminar boundary layers, separated and unseparated, and comparison with numerical computations. *ICAS paper* 84-2.3.1; also *von Kármán Institute Preprint* 84-16.
- DURST, F., MELLING, A. & WHITELAW, J. A. 1976 *Principles and Practice of Laser Doppler Anemometry*. Academic.

- GINOUX, J. J. 1968 Supersonic separated flows over wedges and flares with emphasis on a method of detecting transition. *von Kármán Institute TN 47*.
- GREEN, J. E. 1970 Interactions between shock waves and turbulent boundary layers. *Proc. Aerospace Sci.* **11**, 235–340.
- HAKKINEN, R. J., GREBER, I., TRILLING, L. & ABARBANEL, S. S. 1959 The interaction of an oblique shock wave with a laminar boundary layer. *NASA Memo 2-18-59 W*.
- HANIN, M., WOLFSHTEIN, M. & LANDAU, U. E. 1974 Numerical solution of Navier–Stokes equations for interaction of shock wave with laminar boundary layer. *ICAS 74-17*.
- HANKEY, W. L. & HOLDEN, M. S. 1975 Two dimensional shock wave boundary layer interactions in high speed flows. *AGARDograph 203*.
- KUBOTA, T. & KO, D. R. S. 1967 A second order weak interaction expansion for moderately hypersonic flow past a flat plate. *AIAA J.* **5** (10), 1915–1917.
- LEES, L. & REEVES, B. L. 1964 Supersonic separated and reattaching flows. Part 1. General theory and application to adiabatic boundary layers/shock wave interactions. *AIAA J.* **2** (11), 1907–1920.
- LEWIS, J. E., KUBOTA, T. & LEES, L. 1968 Experimental investigation of supersonic, laminar, two-dimensional boundary layer separation in a compression corner with and without cooling. *AIAA J.* **6** (1), 7–14.
- MACCORMACK, R. W. 1971 Numerical solution of the interaction of a shock wave with a laminar boundary layer. In *Proc. 2nd Intl Conf. on Num. Methods in Fluid Dyn., Univ. of California, 1970*. Lecture Notes in Physics, vol. 8, pp. 151–163. Springer.
- MACCORMACK, R. W. 1982 A numerical method for solving the equations of compressible viscous flow. *AIAA J.* **20** (9), 1275–1281.
- MODARRESS, D. & JOHNSON, D. A. 1979 Investigation of turbulent boundary layer separation using laser velocimetry. *AIAA J.* **17** (7), 707–792.
- REDA, D. C. & MURPHY, J. D. 1973*a* Shock wave/turbulent boundary layer interactions in rectangular channels. *AIAA J.* **11** (2), 139–140.
- REDA, D. C. & MURPHY, J. D. 1973*b* Sidewall boundary layer influence on shock wave/turbulent boundary layer interactions. *AIAA J.* **11** (10), 1367–1368.
- SCHÜTZ, N. S. 1985 Effect of seeding particle size on LDV measurements in a compressible boundary layer. *von Kármán Institute PR 1985-06*.
- SFEIR, A. A. 1970 Interaction d'une couche limite laminaire avec une onde de choc dans un coin de compression. *Rev. Roum. Sci. Tech. Méc. Appl.* **15** (6), 1375–1391.
- SKOGLUND, U. J. & GAY, B. D. 1969 Improved numerical techniques and solution of a separated interaction of an oblique shock wave and a laminar boundary layer. *Research Rep. ME41(69)-068*, Bureau of Engng, University of New Mexico, USA.
- THOMAS, P. D. 1979 Numerical method for predicting flow characteristics and performance of non-axisymmetric nozzles. Theory. *NASA CR 3147*.
- VORROPOULOS, G. & WENDT, J. E. 1983 Laser velocimetry study of compressibility effects on the flow field of a delta wing. In *Aerodynamics of Vortical Type Flows in Three Dimensions. AGARD CP 343*, paper 9; also *von Kármán Institute Preprint 1983-15*.
- WARMING, R. F. & BEAM, R. M. 1978 On the construction and application of implicit factored schemes for conservation laws. *SIAM-AMS Proc.* vol. 11, pp. 85–129.
- WARMING, R. F. & BEAM, R. M. 1979 An extension of A-stability to alternating direction implicit methods. *BIT* **19**, 345–417.